Polarization-sensitive spectral-domain optical coherence tomography using a multi-line single camera spectrometer

Cheol Song,* MyoungKi Ahn and DaeGab Gweon

Nano-Opto-Mechatronics Lab., Department of Mechanical Engineering,
Korea Advanced Institute of Science and Technology (KAIST), Daejeon, Republic of Korea
**feloveyou@kaist.ac.kr*

Abstract: We describe a polarization sensitive spectral domain optical coherence tomography technique based on a single camera spectrometer that includes a multiplexed custom grating, camera lenses, and a high-speed three-line CCD camera. Two orthogonally polarized beams could be separately taken by two lines of the camera as a result of vertically different incident angles. The system could provide the imaging capabilities of a full camera speed and increased measurable depth. The proposed optical coherence tomography system could make a distinction between the normal muscle and cancerous tissue from the chest of a DSred GFP mouse and the OCT images were compared with those of *in vivo* confocal microscopy.

OCIS codes: (170.4500) Optical Coherence Tomography; (230.5440) Polarization sensitive devices; (170.4580) Optical diagnostics for medicine

References and links

1. D. Huang, E. A. Swanson, C. P. Lin, J. S. Schuman, W. G. Stinson, W. Chang, M. R. Hee, T. Flotte, K. Gregory, C. A. Puliafito, and J. G. Fujimoto, "Optical coherence tomography," Science **254**(5035), 1178–1181 (1991).
2. G. Häusler, and M. W. Lindner, "Coherence radar and spectral radar - new tools for dermatological diagnosis," J. Biomed. Opt. **3**(1), 21–31 (1998).
3. J. F. de Boer, B. Cense, B. H. Park, M. C. Pierce, G. J. Tearney, and B. E. Bouma, "Improved signal-to-noise ratio in spectral-domain compared with time-domain optical coherence tomography," Opt. Lett. **28**(21), 2067–2069 (2003).
4. R. Leitgeb, C. K. Hitzenberger, and A. F. Fercher, "Performance of fourier domain vs. time domain optical coherence tomography," Opt. Express **11**(8), 889–894 (2003).
5. J. F. de Boer, T. E. Milner, M. J. C. van Gemert, and J. S. Nelson, "Two-dimensional birefringence imaging in biological tissue by polarization-sensitive optical coherence tomography," Opt. Lett. **22**(12), 934–936 (1997).
6. J. F. De Boer, S. M. Srinivas, A. Malekafzali, Z. Chen, and J. S. Nelson, "Imaging thermally damaged by polarization-sensitive optical coherence tomography," Opt. Express **3**(6), 212–218 (1998).
7. M. J. Everett, K. Schoenenberger, B. W. Colston, Jr., and L. B. Da Silva, "Birefringence characterization of biological tissue by use of optical coherence tomography," Opt. Lett. **23**(3), 228–230 (1998).
8. J. F. de Boer, S. M. Srinivas, B. H. Park, T. H. Pham, Z. Chen, T. E. Milner, and J. S. Nelson, "Polarization effects in optical coherence tomography of various biological tissues," IEEE J. Sel. Top. Quantum Electron. **5**(4), 1200–1204 (1999).
9. M. G. Ducros, J. F. de Boer, H.-E. Huang, L. C. Chao, Z. Chen, J. S. Nelson, T. E. Milner, and H. G. Rylander III, "Polarization sensitive optical coherence tomography of the rabbit eye," IEEE J. Sel. Top. Quantum Electron. **5**(4), 1159–1167 (1999).
10. S. Yazdanfar, M. D. Kulkarni, and J. A. Izatt, "High resolution imaging of *in vivo* cardiac dynamics using color Doppler optical coherence tomography," Opt. Express **1**(13), 424–431 (1997).
11. Z. Chen, Y. Zhao, S. M. Srinivas, J. S. Nelson, N. Prakash, and R. D. Frostig, "Optical Doppler tomography," IEEE J. Sel. Top. Quantum Electron. **5**(4), 1134–1142 (1999).
12. Y. Wang, A. Fawzi, O. Tan, J. Gil-Flamer, and D. Huang, "Retinal blood flow detection in diabetic patients by Doppler Fourier domain optical coherence tomography," Opt. Express **17**(5), 4061–4073 (2009).
13. U. Morgner, W. Drexler, F. X. Kärtner, X. D. Li, C. Pitris, E. P. Ippen, and J. G. Fujimoto, "Spectroscopic optical coherence tomography," Opt. Lett. **25**(2), 111–113 (2000).
14. C. Xu, C. Vinegoni, T. S. Ralston, W. Luo, W. Tan, and S. A. Boppart, "Spectroscopic spectral-domain optical coherence microscopy," Opt. Lett. **31**(8), 1079–1081 (2006).

#135831 - $15.00 USD Received 29 Sep 2010; revised 17 Oct 2010; accepted 22 Oct 2010; published 27 Oct 2010

15. F. Robles, R. N. Graf, and A. Wax, "Dual window method for processing spectroscopic optical coherence tomography signals with simultaneously high spectral and temporal resolution," Opt. Express **17**(8), 6799–6812 (2009).
16. J. Yi, J. Gong, and X. Li, "Analyzing absorption and scattering spectra of micro-scale structures with spectroscopic optical coherence tomography," Opt. Express **17**(15), 13157–13167 (2009).
17. M. R. Hee, D. Huang, E. A. Swanson, and J. G. Fujimoto, "Polarization-sensitive low-coherence reflectometer for birefringence characterization and ranging," J. Opt. Soc. Am. B **9**(6), 903–908 (1992).
18. Y. Yasuno, S. Makita, Y. Sutoh, M. Itoh, and T. Yatagai, "Birefringence imaging of human skin by polarization-sensitive spectral interferometric optical coherence tomography," Opt. Lett. **27**(20), 1803–1805 (2002).
19. E. Götzinger, M. Pircher, and C. K. Hitzenberger, "High speed spectral domain polarization sensitive optical coherence tomography of the human retina," Opt. Express **13**(25), 10217–10229 (2005).
20. B. Baumann, E. Götzinger, M. Pircher, and C. K. Hitzenberger, "Single camera based spectral domain polarization sensitive optical coherence tomography," Opt. Express **15**(3), 1054–1063 (2007).
21. B. Cense, M. Mujat, T. C. Chen, B. H. Park, and J. F. de Boer, "Polarization-sensitive spectral-domain optical coherence tomography using a single line scan camera," Opt. Express **15**(5), 2421–2431 (2007).
22. M. Zhao, and J. A. Izatt, "Single-camera sequential-scan-based polarization-sensitive SDOCT for retinal imaging," Opt. Lett. **34**(2), 205–207 (2009).
23. S.-W. Lee, H.-W. Jeong, and B.-M. Kim, "High-speed spectral domain polarization-sensitive optical coherence tomography using a single camera and an optical switch at 1.3 μm," J. Biomed. Opt. **15**(1), 010501 (2010).
24. C. Fan, Y. Wang, and R. K. Wang, "Spectral domain polarization sensitive optical coherence tomography achieved by single camera detection," Opt. Express **15**(13), 7950–7961 (2007).
25. T. Schmoll, E. Götzinger, M. Pircher, C. K. Hitzenberger, and R. A. Leitgeb, "Single-camera polarization-sensitive spectral-domain OCT by spatial frequency encoding," Opt. Lett. **35**(2), 241–243 (2010).
26. N. Nassif, B. Cense, B. H. Park, S. H. Yun, T. C. Chen, B. E. Bouma, G. J. Tearney, and J. F. de Boer, "In vivo human retinal imaging by ultrahigh-speed spectral domain optical coherence tomography," Opt. Lett. **29**(5), 480–482 (2004).
27. K. Schoenenberger, B. W. Colston, Jr., D. J. Maitland, L. B. Da Silva, and M. J. Everett, "Mapping of birefringence and thermal damage in tissue by use of polarization-sensitive optical coherence tomography," Appl. Opt. **37**(25), 6026–6036 (1998).
28. C. K. Hitzenberger, E. Goetzinger, M. Sticker, M. Pircher, and A. F. Fercher, "Measurement and imaging of birefringence and optic axis orientation by phase resolved polarization sensitive optical coherence tomography," Opt. Express **9**(13), 780–790 (2001).
29. M. Mujat, B. H. Park, B. Cense, T. C. Chen, and J. F. de Boer, "Autocalibration of spectral-domain optical coherence tomography spectrometers for in vivo quantitative retinal nerve fiber layer birefringence determination," J. Biomed. Opt. **12**(4), 041205 (2007).
30. A. B. Shafer, L. R. Megill, and L. Droppleman, "Optimization of the Czerny-Turner spectrometer," J. Opt. Soc. Am. **54**(7), 879–887 (1964).
31. D. R. Austin, T. Witting, and I. A. Walmsley, "Broadband astigmatism-free Czerny-Turner imaging spectrometer using spherical mirrors," Appl. Opt. **48**(19), 3846–3853 (2009).
32. www.ondaxinc.com
33. L. Carretero, M. Ulibarrena, P. Acebal, S. Blaya, R. Madrigal, and A. Fimia, "Multiplexed holographic gratings for fabricating 3D photonic crystals in BB640 photographic emulsions," Opt. Express **12**(13), 2903–2908 (2004).
34. S. Massenot, J.-L. Kaiser, M. C. Perez, R. Chevallier, and J. L. de Bougrenet de la Tocnaye, "Multiplexed holographic transmission gratings recorded in holographic polymer-dispersed liquid crystals: static and dynamic studies," Appl. Opt. **44**(25), 5273–5280 (2005).

1. Introduction

Optical coherence tomography (OCT) is a promising imaging technique that generates high-resolution cross-sectional non-invasive images of sample architectures [1]. With spectral domain OCT (SD-OCT), it is possible to take a depth profile by a single camera image, whereas time domain optical coherence tomography requires mechanical depth scanning. The depth information in SD-OCT is accomplished through the Fourier transform of the interference signal [2]. Recently, improved sensitivity and signal to noise ratio (SNR) have advanced various studies in SD-OCT [3,4]. However, conventional SD-OCT can only afford an intensity-based cross-sectional image to show architectural morphology. Although it could obtain morphological structures from the sample, such data is often insufficient to offer crucial information required for some pathologies and material analysis applications. Thus, much effort has been applied toward the contrast imaging based on the characteristics of the light, such as the polarization [5–9], the Doppler Effect [10–12], and the spectroscopic features and absorption [13–16]. Particularly, polarization-sensitive optical coherence tomography (PS-OCT) utilizes the polarization properties of back-reflected light to obtain

#135831 - $15.00 USD Received 29 Sep 2010; revised 17 Oct 2010; accepted 22 Oct 2010; published 27 Oct 2010

biochemical information in addition to the morphological feature. The first time domain PS-OCT was implemented using the free-space Michelson interferometer [17]. In the first application of spectral domain based PS-OCT, experimental measurements were fulfilled using several polarization states, which yielded 4 or 16 final images containing the Müller matrix element information from the biological tissue, while the image acquisition speed was very slow due to the one-dimensional mechanical lateral scanning [18]. In 2005, high-speed polarization sensitive spectral domain optical coherence tomography (PS SD-OCT) was demonstrated using two detection channels [19]. Two spectrometers that operated in parallel at 20,000 A-lines/s each acquired two orthogonally polarized interference signals. However, the system had some difficulties in terms of the high-precision alignment of the spectrometers, the exact trigger timing and synchronization, and the system complexity.

Therefore, several PS SD-OCT techniques based on a single camera spectrometer have recently become of increased interest [20–25]; they measure the polarized interference beams at different detection positions [20,21], polarization states [22], times [23], and signal processing domains [24,25]. The spectra of the horizontal and vertical polarization channels were measured in an adjacent geometry with 1024 pixels for each channel [20]. The scheme comprising a phase modulator and a custom-built Wollaston prism at the spectrometer was also presented [21]. However, these systems had a reduced number of pixels available for each spectrum, which in turn reduced the measurable depth range. Electro-optic modulator (EOM) was employed for detection of various polarization states [22]. Also, an optical switch enabled to acquire the interference signals at 1.3 μm in turn, enduring a loss of full imaging speed [23]. Also, custom-built reference delay line assembly entailed the acquisition and processing of the PS-OCT signals on two Fourier domains [24]. However, these schemes could limit the image acquisition rate. More recently, the spatial frequency encoding based on an EOM with four-step modulation was applied to PS SD-OCT [25].

Most previous studies of single camera spectrometers suffer from the reduced imaging speed or depth. Here, we propose a PS SD-OCT technique using a single camera spectrometer that includes a custom-built multiplexed grating and a three-line CCD camera. The novel spectrometer, composed of a single camera with more than two separated lines can independently acquire two orthogonally polarized interference signals. This approach secures a full imaging speed determined by the maximum line rate of the CCD camera and the maximal imaging depth via the spectrometer resolution. The system measured birefringent biological tissues, such as human palm and mouse chest muscle. In addition, the differences between normal muscle and abnormal tissue, such as Lewis lung carcinoma (LLC), were verified by complementary confocal microscopy studies in addition to the PS SD-OCT system.

2. Design of the system

2.1 System description

A schematic diagram of the PS SD-OCT instrument based on a three-line single camera spectrometer is shown in Fig. 1. The suggested system is composed of a broadband light source, a reference arm, a sample arm, and a novel spectrometer for detection. A broad lighter (Broad lighter D830-HP1, Superlum Ireland) are employed, which is a very low coherence light source based on a combination of two pigtailed superluminescent diode (SLD) modules' emission using single mode fiber couplers. The power and operating mode of the SLD laser source are controlled via the RS-232 interface. Two superluminescent diode modules with different emission spectra and an average output power of 7.82 mW are employed. The output beam emitted from the superluminescent diode laser is centered at a wavelength of 826.4 nm with a bandwidth of 84.7 nm. The broadband light source yields a theoretical axial resolution of less than 4 μm. Initially, the output beam with an aperture size of 2 mm is horizontally polarized by a linear polarizer. The polarized beam is divided by a non-polarizing beam

#135831 - $15.00 USD Received 29 Sep 2010; revised 17 Oct 2010; accepted 22 Oct 2010; published 27 Oct 2010

splitter (NPBS) into a reference and a probe beam. Two quarter wave plates (QWP) determine the polarization states in both arms of the Michelson interferometer.

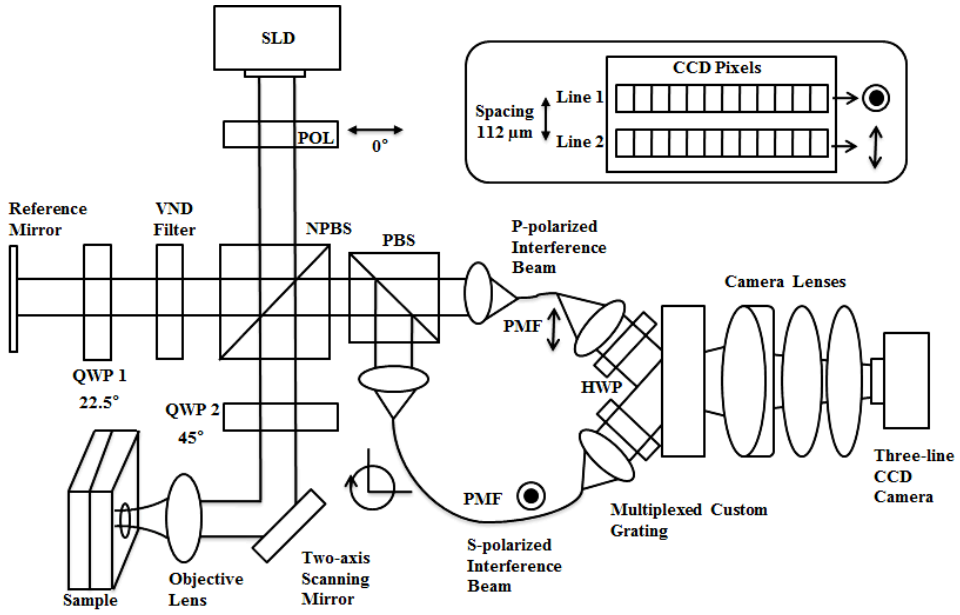

Fig. 1. Schematic diagram of the polarization-sensitive spectral domain optical coherence tomography system using a single camera spectrometer. The system was composed of a broadband superluminescent diode laser (SLD), a Michelson interferometer that used polarization optics, and a home-built spectrometer, including a high-speed camera module and camera lenses. The POL (linear polarizer), NPBS (non-polarizing beam splitter), PBS (polarizing cube beam splitter), VND filter (variable neutral density filter), QWP (quarter wave plate), PMF (polarization maintaining fiber), and HWP (half wave plate) are indicated.

The reference beam is transmitted at an intensity that was twice that passed by the quarter wave plate oriented at 22.5°. The reference beam is, therefore, linearly polarized at 45°, which provided the same reference power in two detection channels of the spectrometer. The reference beam contains p-polarized and s-polarized beam components with the same amplitude and phase. Additionally, the reference beam is reflected by a reference mirror after passing through a variable neutral density filter (ND filter), which is used to adjust the power of the reference beam and, correspondingly, the power of probe beam, in order to maximize the SNR. The probe beam passes through a quarter wave plate (QWP) oriented 45° with respect to the horizontal axis, which delivers a circularly polarized beam to the sample. The circularly polarized probe beam responds to the birefringent sample, which includes an optical axis in a plane perpendicular to the direction of the propagation beam. The focal length of the objective lens determines the field of view and the lateral resolution. The reference beam interferes with the probe beam that was backscattered or back-reflected from each layer of the sample after recombination at the NPBS. After passing through the NPBS, the interference beams are divided into two polarization beams, p-polarized and s-polarized, by the polarizing beam splitter (PBS). Two orthogonally polarized beams are directed into two polarization-maintaining fibers (PMF) and directed toward the home-built single camera spectrometer, which includes a three-line CCD camera. To collect only one polarization mode in each PMF, the birefringent axes of two PMFs are aligned parallel to the p-polarized and s-polarized incoming beams. Two half-wave plates (HWP) are incorporated in front of the transmission grating to maximize the diffraction efficiency of the transmission grating. After two orthogonally polarized interference beams are detected by the three-line CCD camera, post-processing procedures are applied. The CCD pixel sequences between the p-polarized and

#135831 - $15.00 USD Received 29 Sep 2010; revised 17 Oct 2010; accepted 22 Oct 2010; published 27 Oct 2010

s-polarized channels are reversed due to the different incident angles (+ 59.428°, –59.428°) with respect to the normal surface of the multiplexed grating.

The proposed PS SD-OCT system included two imaging steps, image acquisition and post-processing. Custom-written Visual C + + image acquisition software was incorporated into the data collection routine. Two-dimensional raw data (2048 x 1024 pixels/frame) from two orthogonal interference spectra were saved at a rate of about 8.98 frames per second (maximum line rate of 9.2 kHz) using a high-speed frame grabber (i2S, Horizon Link) or a camera link frame grabber (Solios 6M CL E, Matrox). Only 2048 pixels of line data, among 2098 pixels, were retained for the Fourier transformation due to the power-of-two length requirement and data acquisition technicalities that arose in the algorithm. The camera was operated at a pixel clock speed of 20 MHz in triple 8 bit output mode with an external edge trigger mode. The acquisition of two orthogonally polarized interference beams was easily accomplished using a single camera control signal. The synchronization between a three-line camera and the scanning mirror was achieved using a reference clock signal composed of a counter output pulse train derived from a multi-function board (PCI 6281, National Instruments). The input control signal of the scanning mirror (6230XY, Cambridge Corp.) was a saw-tooth wave with a cosine wave retraced signal.

The axial scan spectra contained DC term and autocorrelation noise after application of the Fourier transform, which degraded the final image quality. Fixed pattern noise was removed by subtracting the ensemble average of all axial scan results from each axial scan spectrum prior to Fourier transformation. The scheme used to remove the fixed pattern noise was similar to that presented by Nassif et al. [26]. Next, the axial scan data acquired on the line CCD were evenly sampled in the wavelength domain and, therefore, were evenly sampled by linear interpolation and re-sampling in the wavenumber domain for wavelength assignment. The accuracy of the polarization-sensitive imaging data was increased by zero padding. Noise below a certain intensity level resulted in severe phase retardation and fast axis orientation artifacts [27]. Therefore, only data above a certain threshold were processed to obtain the reflectivity, phase retardation, and fast axis orientation from the birefringent sample [28]. Two interference signals yielded the reflectivity (R), phase retardation (δ), and cumulative fast axis orientation (θ) using the following formulae:

$$R(z) \propto \left[A_H(z)\right]^2 + \left[A_V(z)\right]^2 = I_H(z) + I_V(z) \tag{1}$$

$$\delta(z) = \arctan\left[\frac{A_H(z)}{A_V(z)}\right] = \arctan\left[\sqrt{\frac{I_H(z)}{I_V(z)}}\right] \tag{2}$$

$$\theta = \frac{180^\circ - \Delta\Phi}{2}, \quad \Delta\Phi = \Phi_H - \Phi_V \tag{3}$$

The unambiguous ranges are 90° for δ and 180° for θ. All images were finally obtained after median filtering to reduce the speckle noise. The two interference spectra were independently obtained at different detection lines of the spectrometer. The retardation and fast axis orientation are quite sensitive to the amplitude and phase of the measured interference signals. So, the alignment to keep the constant phase difference from the two spectra along the depth was basically achieved by adjusting one of two incident beam angles [19]. In addition, the correspondence between two axial peaks is essential because the discrepancy can lead to polarization artifacts. In the step of wavelength assignments mentioned above, therefore, the iterative scheme for pixel to pixel correspondence between two axial spectra was applied on the basis of the wavelength assignment using a cover glass plate in the source arm [29].

#135831 - $15.00 USD Received 29 Sep 2010; revised 17 Oct 2010; accepted 22 Oct 2010; published 27 Oct 2010

2.2 Design of the spectrometer

Current commercial spectrometers or monochromators based on the Czerny–Turner configuration usually utilize a reflection grating, slits, focusing, and collimating spherical mirrors [30]. The Czerny–Turner spectrometer can simultaneously acquire a broadband spectrum, is compact in size, and is easy to align [31]. Diffraction gratings are usually divided into two types: reflection (surface relief grating, SRG) or transmission (volume phase holographic grating, VPHG). VPHGs have low stray light detection and low visible and NIR absorption cross-sections. They are sealed in glass, which increases their longevity, facilitates handling, renders them scratch-resistant, and makes them easy to clean [32]. The diffraction efficiency (DE), defined as the ratio of the power in the diffracted beam to the power in the incident beam, depends on the wavelength and the polarization. The diffraction efficiency of a commercial VPHG at a center wavelength of 830 nm is generally 90%, although the efficiencies may differ by 10%, depending on the polarization state. The achievable performance and grating strength were limited by the material dynamic range and the number of multiplexed gratings. One of the most crucial and unique features of the VPHGs is their multiplexing capabilities [33,34]. It is possible to include multiple VPHGs within a given volume that operate independently and do not interfere with each other within the limited range of wavelength and angles through which diffraction occurs.

The spectrometer design was very important in the proposed PS SD-OCT. The essential components of the spectrometer were the grating and the detection camera. The home-built spectrometer included a multiplexed transmission custom grating (1050 lines/mm, Wasatch Photonics), a three-element air-spaced camera lens, and a three-line CCD camera (2098 pixels x 3 lines). We utilized a CCD camera containing three lines (Basler Vision Technology L301k, 2098 elements per line, pixel size 14 μm x 14 μm), and the center-to-center spacing between lines was 112 μm. The camera was mounted on a three-axis translation and two-axis rotation stage.

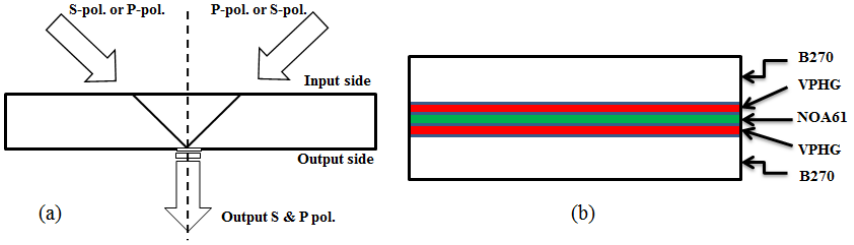

Fig. 2. Schematic of multiplexed custom transmission grating. (a) Orientation. (b) Cross section.

In this study, two types of VPHG were constructed and laminated together in an attempt to produce the desired multiplexed grating. Because two VPHGs were polarization-dependent from each other, it was necessary to reduce the cross-talk. When the two gratings were combined, the overall diffraction efficiencies were dependent on the differences between the polarization efficiencies of two VPHGs. Figure 2(a) illustrates the multiplexed transmission grating, 25 mm x 25 mm in size, which was custom-built by Wasatch Photonics, Inc. A cross-section of the multiplexed grating is shown schematically in Fig. 2(b). The grating with a 3 mm substrate has a total thickness of 6 mm. This thickness yielded a higher wave-front tolerance than did the 1 mm substrate. A broadband antireflective (AR) coating for wavelengths between 760 nm and 880 nm was applied to each side of the grating to reduce reflectivity to < 1%. Without the AR coating, a large fraction of the incident light was lost, particularly the s-polarized light, due to the higher incident angle. Also in this case, cavity effects arose from two beams, which exited the last surface normal to the surface, as designed by Wasatch Photonics, Inc. The input side of the grating had a working angle of 52.9 – 67.5°,

#135831 - $15.00 USD Received 29 Sep 2010; revised 17 Oct 2010; accepted 22 Oct 2010; published 27 Oct 2010

centered at 59.428°, as illustrated by the dispersion of the grating shown in Fig. 3(a). Because these gratings were not symmetrical, the dispersion was not linear and these values could be calculated using the grating equation. The output side of the grating had a working angle of –3.6 to + 3.6 ° centered at 0°.

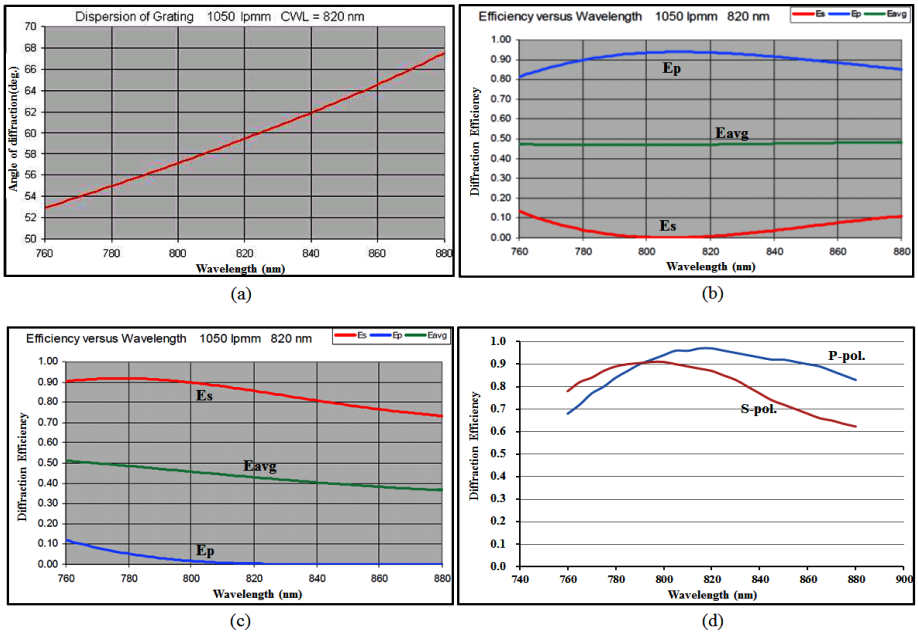

Fig. 3. Characteristics of multiplexed custom transmission grating. (a) Dispersion of the grating. (b) Diffraction efficiencies in p-polarized dependent grating. (c) Diffraction efficiencies in s-polarized dependent grating. (d) Calculated overall efficiencies.

Figures 3(b) and 3(c) show the diffraction efficiencies as a function of wavelength in the p-polarized dependent grating and the s-polarized dependent grating. Any residual polarization in one grating was subtracted from the other grating, and this determined the overall efficiency. For example, graph (b) in Fig. 3 shows the p-polarized light diffraction to be 81% efficient at 760 nm, while graph (c) shows the p-polarized light diffraction to be 11% efficient at 760 nm. This implies that the overall efficiency approached 70% for p-polarized light at 760 nm. The transmission efficiencies of two polarized beams exceeded 75% at the center wavelength. Therefore, the overall efficiency of the multiplexed custom grating was determined as shown in Fig. 3(d). The values approached an average of 80%. Experimental measurements of the diffraction efficiency are time-consuming processes with high associated costs. The experimental first-order efficiencies at 828 nm were provided by the manufacturer (86% for p-polarized light, 74% for s-polarized light). A comparison of these values and the calculated efficiencies yielded a difference of about 10%, which did not critically affect the spectrometer performance. Figures 4(a) and 4(b) show schematic diagrams of the novel spectrometer viewed from an upward perspective. The incident angles of ± 60° were measured off the normal to the surface of the multiplexed grating. The aperture size of the incoming collimation beam was 10 mm. As shown in Fig. 4(c), after passing through the multiplexed grating, two incident beams followed slightly different optical paths. However, two polarization interference beams arrived on different line pixels because the incident angles have a change of only a small amount ($\alpha = 0.0266°$). Two collimators were mounted on the precision kinematic optical mounts. The incidence angles of two collimators were accurately adjusted by three kinematic screws. The camera lenses were composed of a commercial NIR achromatic doublet lens (Edmunds) and two designed singlet lenses. The

#135831 - $15.00 USD Received 29 Sep 2010; revised 17 Oct 2010; accepted 22 Oct 2010; published 27 Oct 2010

total length from the grating to CCD pixel was 162 mm. The effective focal length of three camera lenses was 120 mm; the numerical aperture in the image space was 0.055. A plot of the root-mean-square (RMS) wave-front error as a function of the wavelength (Fig. 5(a)) disclosed that the value was much lower than the diffraction-limited value. The different incidence angle did not critically change the spectrometer performance, as proved by commercial optical design software (Fig. 5(b)).

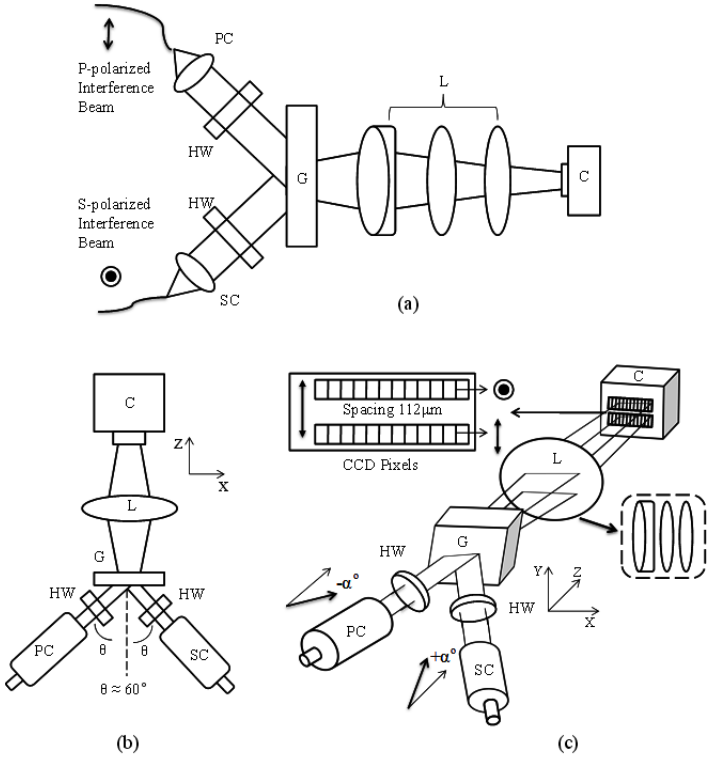

Fig. 4. Schematic diagrams of the proposed spectrometer. The PC (P-pol. collimator), SC (S-pol. collimator), G (Multiplexed grating), L (Camera lens), C (Multi-line camera), and HW (Half-wave plate) are indicated. (a) Home-built spectrometer. (b) Upward view. (c) Isometric view.

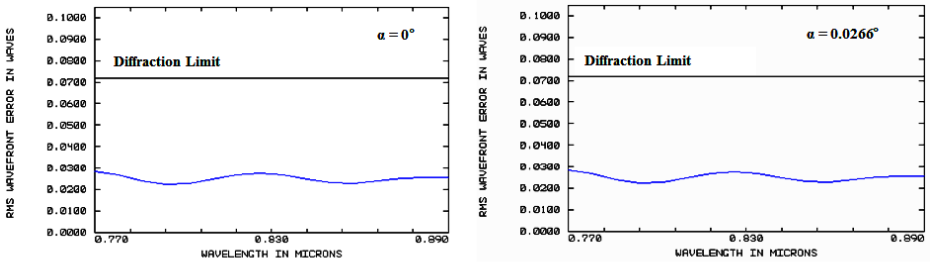

Fig. 5. RMS wave-front errors along the wavelength predicted by ZEMAX. (a) Incidence angle, 0°. (b) Incidence angle, 0.0266°.

#135831 - $15.00 USD Received 29 Sep 2010; revised 17 Oct 2010; accepted 22 Oct 2010; published 27 Oct 2010

3. Results

The theoretical axial resolution of 3.5 μm (in air) was determined by the performance of the optical source. However, the spectral shape of the laser source was not perfectly Gaussian, and the axial resolution was decreased. The axial performance was experimentally assessed by adjusting the quarter wave plate in the sample arm to the same orientation as that in the reference arm, with a fast axis angle of 22.5° with respect to the horizontal axis. Figure 6(a) shows the full width at half maximum (FWHM) of the normalized axial point spread function measured along the depth. The results generally show the decay of the depth dependent axial resolution. The average FWHM over the whole depth range is 3.96 μm of the s-polarized beam and 3.89 μm of the p-polarized beam, respectively. The resolution differed for each polarization state due to the spectrometer alignment and imperfections in the polarizing optics that were magnified by the broadband laser spectrum. And a mirror and a wave plate at different wavelength were implemented in the sample arm as a test sample to prove the system performance. Phase retardation and fast axis orientation were measured along the depth as shown in Fig. 6(b). Two values are located in a constant over the whole depth range, and the deviations of phase retardation values were much smaller than axis orientation. The performance would generally get worse along the depth as a result of poor signal quality.

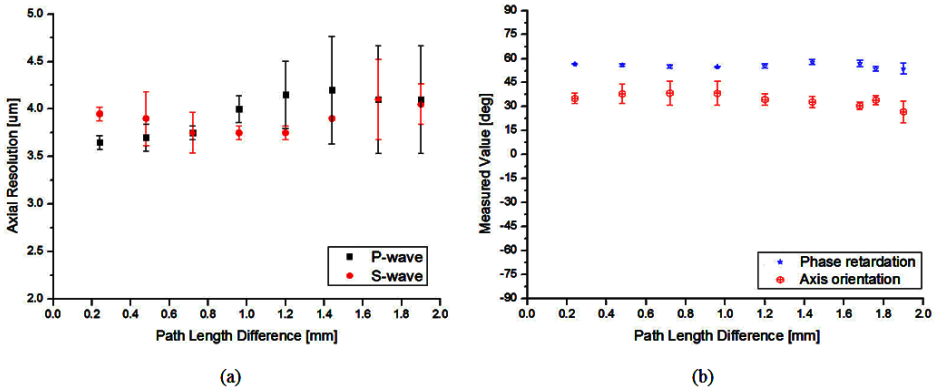

Fig. 6. The measured system performance. (a) Axial resolution of two orthogonal polarization states as a function of the depth. (b) Phase retardation (δ) and axis orientation (θ) measured along the depth, by using a combination of a quarter wave plate and a mirror. Here, error bars denote the standard deviation.

The lateral resolution of the OCT system was determined by the numerical aperture of the objective lens, as in conventional optical microscopy. The objective lens with focal length of 19 mm yielded a lateral resolution of 10 μm and a lateral scanning range of 2.5 mm. In addition, when two orthogonally polarized interference beams were focused by the designed air-spaced triple lenses onto the CCD pixels, the maximum imaging depth range was 1.9 mm in air due to the resolution of the spectrometer, 0.09 nm. The sensitivity of our system at various depths was evaluated using the ideal reflector. The system sensitivity of 95.2 dB was measured with an integration time of 108 μsec. It was dropped by approximately 9 dB at a 2/3 distance within a total depth range due to the finite pixel resolution of the spectrometer.

The retardation images show the retardation values between the two orthogonal polarization components displayed in color-coding from 0° (purple) to 90° (red). If the sample was non-birefringent, no phase retardation was observed (0°, purple). A value of 90° (red) corresponded to a phase lag of a quarter wavelengths between two orthogonal polarization directions due to birefringence. Also, images of the fast optical axis orientation were displayed as color-coded from –90° (purple) to 90° (red). Birefringence assessment of the

#135831 - $15.00 USD Received 29 Sep 2010; revised 17 Oct 2010; accepted 22 Oct 2010; published 27 Oct 2010

human palm was achieved as illustrated in Fig. 7. The dermis layers in the human palm were birefringent due to the presence of collagen, whereas the sweat gland was not birefringent due to the abundance of empty space.

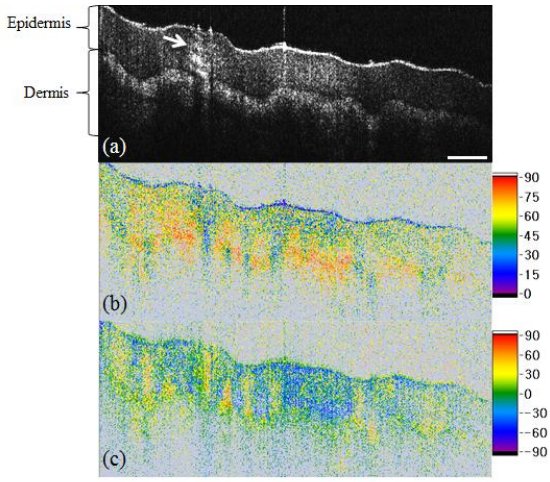

Fig. 7. *In-vivo* PS-OCT scans of human palm. The white arrow represents the sweat duct of human palm. (a) Reflectivity image (logarithmic scale). (b) Phase retardation image (color, °). (c) Cumulative fast axis orientation image (color, °). The scale bar is 250 μm.

Differences between normal and the cancerous muscles (LLC) from the chest of a DSred GFP mouse were examined by polarization-sensitive imaging. Figure 8 shows the presence of birefringence in the normal mouse muscles along the sample depth. The phase retardation image at a certain depth is displayed in red; the cumulative fast axis orientation due to backscattering just below the top surface at an optical depth of 200 μm is displayed in blue. In contrast, the phase retardation and fast axis orientation images of the LLC are displayed in purple and green, respectively. These results implied that the birefringence in the chest muscle disappeared, and the muscular system was destroyed by the LLC. In normal mouse muscles, laterally organized layer structures were visible in the reflectivity image, while they did not appear in the reflectivity image of the LLC. The speckled artefacts are definitely spread, particularly at the sample surface in the axis orientation image of LLC tissue, due to some influence of a background noise or a limited dynamic range of the PS-OCT signals. The sample tissues were exactly differentiated by the phase retardation and fast axis orientation images of the proposed PS SD-OCT.

#135831 - $15.00 USD Received 29 Sep 2010; revised 17 Oct 2010; accepted 22 Oct 2010; published 27 Oct 2010

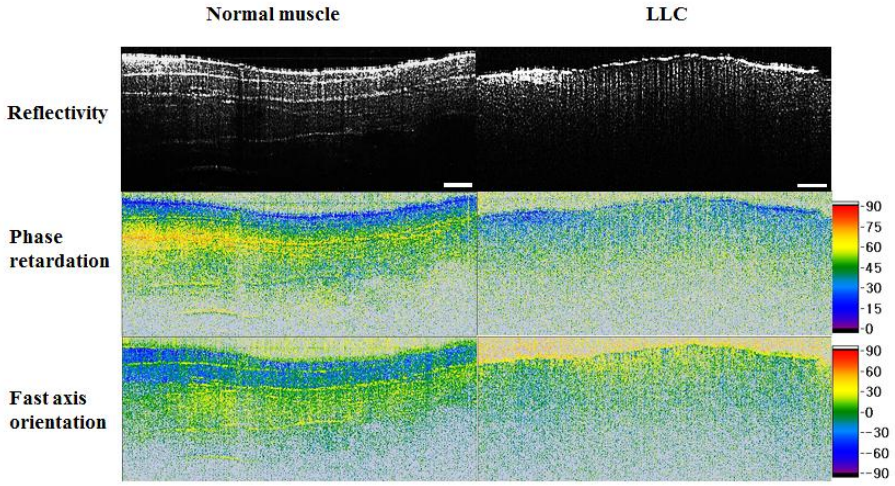

Fig. 8. Comparison between normal chest muscle and LLC of mouse using PS SD-OCT. The image scales are as follows: reflectivity image (logarithmic scale), phase retardation image (color, °) and cumulative fast axis orientation image (color, °). The scale bar is 200 μm.

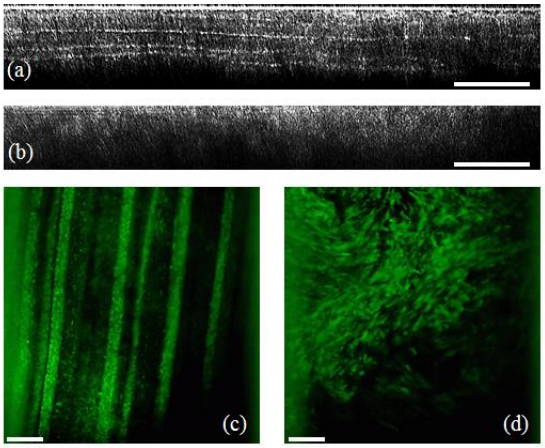

Fig. 9. Reflection and fluorescence images of normal chest muscle and LLC tissues measured by a home-built *in vivo* confocal microscope. (a) Reflection image of normal muscle. (b) Reflection image of LLC. (c) Fluorescence image of normal muscle. (d) Fluorescence image of LLC tissue. The scale bar is 100 μm.

We have confirmed the outstanding results of OCT images as a method of comparing with confocal microscopy images. Reflection and fluorescence images of chest muscle and LLC samples were obtained using a home-built reflection and fluorescence hybrid *in vivo* confocal microscope. In the reflection confocal mode, the confocal microscope used a linearly polarized diode laser with a wavelength of 830 nm. Fluorescence confocal images were acquired using the diode laser with wavelengths of 488 nm. The microscope had a field of view (FOV) of 700 μm x 700 μm with a 20 x objective lens (f = 9 mm). The axial and lateral resolutions for the fluorescence imaging mode (488 nm laser) were 3.4 μm and 490 nm, respectively. In the reflection imaging mode (830 nm laser), the axial and lateral resolutions were 2.75 μm and 780 nm, respectively. The cross-sectional reflection confocal images in Figs. 9(a) and 9(b) were reconstructed from the three-dimensional intensity data. The penetration depth (110–150 μm) of the confocal microscope was lower than that of the OCT system. The reflection confocal image of normal muscle included several parallel layers, in

#135831 - $15.00 USD Received 29 Sep 2010; revised 17 Oct 2010; accepted 22 Oct 2010; published 27 Oct 2010

agreement with the OCT reflectivity image, whereas the reflection image of the LLC sample did not show any distinctive structures. The comparison of the fluorescence and reflection images could reveal the dissimilarity between the normal chest muscle and LLC tissue. Figure 9(c) shows the highly organized layers composed of many fibrous structures, which produced birefringence in the sample, whereas the fluorescence image from the LLC tissue showed amorphous structures, as shown in Fig. 9(d).

4. Discussions

The two orthogonally polarized signals were simultaneously obtained at the different positions of the detector, similar to the dual-camera PS SD-OCT system. So, the proposed system also needs the careful alignment between the two detection channels. However, the spectrometer configuration has great merits except the similarly available depth range and full imaging speed and sensitivity compared to dual-camera system. The system complexity could be rather decreased thanks to the sharing of all components in a spectrometer, in spite of considering additional input beam collimator in the spectrometer. In addition, the exact trigger timing and synchronization required at the dual-camera system could be easily realized by using a control signal.

OCT interferometers can be constructed as free-space or fiber-based systems. Although a free-space interferometer is more difficult to align than a fiber optic system, the polarization state is conserved such that the measured sample birefringence is more accurate. Free-space interferometers that use bulk optical components, such as the proposed system, can more faithfully conserve the polarization state of the light compared to fiber optic-based interferometers. However, the optical components of the free-space interferometer are difficult to align due to the long arm of the interferometer. Misalignment can affect the performance of the implemented system. In this case, the accuracy of the polarization-sensitive measurements could be decreased by the low SNR of the system. Additionally, the SLD source used in this study has very broad spectral bandwidth that the required polarization states could not be perfectly achieved. A system alignment and imperfections in polarization could introduce birefringent artefacts into the measurement images.

The effective focal length of the camera lens was determined with minimal crosstalk between the orthogonally polarized beams. Camera lens with an effective focal length in excess of 200 mm can be utilized to increase the depth range to 3 mm, although the optical power efficiency in the spectrometer would decrease due to the large focal volume. We note that the maximal image acquisition speed of the current system was an A-scan rate of 9.2 kHz. The acquisition rate can be increased by introducing a TDI digital camera (for example, Piranha HS-series, Dalsa Corp.) although the camera lens or multiplexed grating may be exchanged for maximal depth imaging. This camera has a line rate of 36 kHz and a resolution of 4096 x 96 using TDI technology to maximize the photon capture efficiency. For reference, recently available CMOS based dual-line camera has a difficulty in applying to this spectrometer because of the measurement crosstalk caused by no spacing between two-line pixels.

5. Conclusions

In this paper, a PS SD-OCT instrument using a multi-line single camera spectrometer has been successfully demonstrated. The novel spectrometer was composed of a multiplexed transmission grating, air-space three-element designed camera lenses, and a three-line CCD camera. Note that two spectral interferograms were separately recorded by different lines of a three-line CCD camera, two channels of a polarization-sensitive spectrometer. Each polarization channel beam had a vertically different incident angle on the multiplexed custom grating, while the incidence angles of two collimators were horizontally aligned at angles of ± 60° with respect to the multiplexed grating. Also, the system configuration could help to utilize the maximum values of camera imaging speed and the depth range. Without

#135831 - $15.00 USD Received 29 Sep 2010; revised 17 Oct 2010; accepted 22 Oct 2010; published 27 Oct 2010

introducing a time delay, two orthogonally polarized interference beams were simultaneously read out at a rate of 8.98 frames per second, using only a control signal of a multi-line CCD camera. And the sharing components in the spectrometer secure system simplicity compared to two-camera based PS SD-OCT. The axial resolution was experimentally determined to be 3.96 μm for the s-polarized beam and 3.89 μm for the p-polarized beam. The phase retardation image of the human palm tissue showed the presence of collagen in the dermis layers. Moreover, this modality could discriminate the normal chest muscle and LLC tissue from the DSred GFP mouse. The acquired PS-OCT images were analyzed with reflection and fluorescence images from a confocal laser scanning microscope.

Acknowledgements

This work was supported by the middle, position technical development business of Korean Ministry of Commerce, Industry and Energy (#10028350). The authors would like to thank Prof. GouYoung Koh in KAIST for providing us with the normal and LLC tissues.

#135831 - $15.00 USD Received 29 Sep 2010; revised 17 Oct 2010; accepted 22 Oct 2010; published 27 Oct 2010